buildings

MDPI

Article

Experimental Study on the Strength and Microstructure of Red Mud-Based Silty Sand Modified with Lime–Fly Ash

Song Yin [1], Pan Yan [1], Xinming Li [1,*], Yulong Wang [1], Xianwei Zhang [2], Yuzhou Sun [1] and Cheng Chen [2]

[1] School of Civil Engineering and Architecture, Zhongyuan University of Technology, Zhengzhou 450007, China; syin@zut.edu.cn (S.Y.); 2021109360@zut.edu.cn (P.Y.); 2021109349@zut.edu.cn (Y.W.); yuzhousun@126.com (Y.S.)

[2] State Key Laboratory of Geomechanics and Geotechnical Engineering, Institute of Rock and Soil Mechanics, Chinese Academy of Sciences, Wuhan 430071, China; xwzhang@whrsm.ac.cn (X.Z.); cchen@whrsm.ac.cn (C.C.)

* Correspondence: xmli@zut.edu.cn; Tel.: +86-0371-62506735

Abstract: This study aimed to assess the viability of utilizing lime–fly ash (LF) and red mud (RM) in the modification of silty soil (LF-RMS) for subgrade filling. The primary objective of this research was to analyze the mechanical characteristics and examine the curing mechanisms associated with said modified materials. Different curing times were utilized in the analysis of mechanical properties (e.g., via unconfined compression testing), microstructure (via scanning electron microscopy, X-ray diffraction, and thermogravimetric-differential thermal analysis), and environmental indices (via assessment of corrosivity, heavy metal concentration, and radioactivity) with various dosages of red mud (D_{RM}) and Lime–fly ash (D_{LF}). Analyses of the curing mechanisms, failure modes, microstructures, and degrees of environmental impact associated with LF-RMS were also undertaken. The tests indicated that the unconfined compressive strength (UCS) exhibited an initial increase followed by a decrease as the D_{RM} and D_{LF} levels increased. Additionally, the strength of LF-RMS increased with an increase in curing time. It is worth noting that the specimen composed of 20% LF and 23% RM ($D_{20\%LF+23\%RM}$) demonstrated a maximum UCS value of 4.72 MPa after 90 days of curing, which indicates that it has the strongest ability to resist deformation. The strength of the specimen cured for 90 days was 1.4 times higher than that of the specimen cured for 7 days (1.97 MPa). Furthermore, the toxic concentration and radionuclide index of LF-RMS were significantly reduced compared to those of pure RM. The overall concentration of heavy metals in the $D_{20\%LF+23\%RM}$ specimen decreased by more than 60% after curing for 28 days. The internal irradiation index and the external irradiation index decreased by 1.63 and 1.69, respectively. The hydration products in LF-RMS play a key role in the solidification of heavy metals, and the alkaline environment provided by RM also contributes to the precipitation and replacement of heavy metals. In this study, red mud, fly ash and lime were used to modify silty soil. The central tenets of sustainable development may be achieved through the reuse of RM as a road filler.

Keywords: red mud; lime–fly ash; silty soil; road performance; environmental impact

check for updates

Citation: Yin, S.; Yan, P.; Li, X.; Wang, Y.; Zhang, X.; Sun, Y.; Chen, C. Experimental Study on the Strength and Microstructure of Red Mud-Based Silty Sand Modified with Lime–Fly Ash. *Buildings* **2024**, *14*, 1336. https://doi.org/10.3390/buildings14051336

Received: 5 April 2024
Revised: 2 May 2024
Accepted: 6 May 2024
Published: 8 May 2024

Copyright: © 2024 by the authors. Licensee MDPI, Basel, Switzerland. This article is an open access article distributed under the terms and conditions of the Creative Commons Attribution (CC BY) license (https://creativecommons.org/licenses/by/4.0/).

1. Introduction

One byproduct of processing alumina is red mud (RM). Over 5 billion tons of RM are thought to be in storage globally [1,2]. Although the global average rate of RM use is 15%, it is just 4% in China. The resource utilization rate of RM is significantly lower than the average of other forms of industrial solid waste [3,4]. RM is a solid waste containing high levels of alkalinity, heavy metals, and radioactivity. Therefore, long-term stockpiling on a large scale not only wastes land resources but also erodes the surrounding soil and pollutes groundwater [5–7].

RM can be used in large quantities for the construction of roads. RM contains a large number of active substances, and these make up the majority of RM that is utilized in

road construction [8,9]. Moreover, fly ash also exists as a solid waste, and research on its application in road building is relatively mature [10–12]. Through alkali excitation, RM can be combined with other additives for the production of high-strength cementitious materials [13–15]. In recent years, there has been a gradual increase in research into RM as a road construction material. Ma et al. [16] utilized RM as an additive to loess to produce subgrade materials for roads. They found that the unconfined compressive strength (UCS) of the mixture mixed with a 30% RM dosage (D_{RM}) was 1.6 times greater than the UCS of loess of the same age after 28 days of curing. Sarath et al. [17] used fly ash and cement to stabilize RM as a road construction material; their specimens with a fly ash dosage of 20% and a cement dosage of 5% exhibited the largest UCS after 28 days of curing, reaching 2340 kPa. Furthermore, the concentration of toxic metals in the RM fell within an acceptable range. Chandra et al. [18] studied the applicability of RM and fly ash geopolymers as subgrade materials. After 28 days of curing, the UCS of the modified specimen increased by three times. Liu et al. [19] studied the strength characteristics of lime–fly ash (LF)–stabilized Bayer RM using orthogonal tests. The ratio of LF was considered to have the greatest influence on the 7-day unconfined compressive strength of the specimen, and the main factor affecting the 28-day UCS was the chemical composition of the RM. It was further determined that 50% lime and fly ash +70% SRM (from Shandong Aluminum Industry Co., Ltd. (Shandong, China)) +30% soil represented the optimal proportion, and its 7-day UCS was 1.799 MPa; this mixture could therefore be used as subgrade material. The literature indicates that the addition of red mud, fly ash, and lime can significantly enhance the performance of modified materials, allowing relevant requirements of road materials' mechanical properties and environmental consequences to be met. However, there is a lack of research on the strength attributes and microstructure of materials simultaneously modified with red mud, fly ash, and lime. Furthermore, it is important that we further investigate whether the environmental impact and the strength of these modified materials fulfil certain criteria for road filling. Therefore, this study aims to explore the feasibility of using lime–fly ash and red mud-modified silty sand (LF-RMS) for subgrade construction and deter-mine the optimal material ratio for maximizing mechanical properties while minimizing environmental impact. Unconfined compressive strength (UCS) tests were conducted on specimens with varied RM dosages (D_{RM}), LF dosages (D_{LF}), and curing times to determine the best D_{RM} and D_{LF}. Furthermore, X-ray diffraction (XRD), thermogravimetric-differential thermal analysis (TG-DTG), and scanning electron microscopy (SEM) were used to examine the hydration products and microstructure of LF-RMS. Finally, the heavy metal leaching concentration and radioactivity of LF-RMS were detected to evaluate its environmental impact. This research will contribute to enhancing the efficiency of red mud utilization and will play a positive role in environmental protection. A flowchart of this research study is shown in Figure 1.

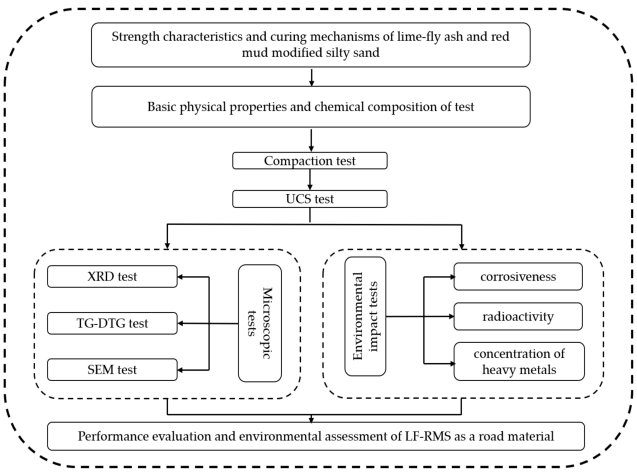


Figure 1. Flowchart.

2. Materials and Methods

2.1. Materials

In this study, Bayer red mud (RM) and lime–fly ash (LF) were used to modify silty soil (referred to as LF-RMS). The silty soil was taken from Zhengzhou, Henan Province, China, and the specimens were yellow–brown. RM was provided in block form by a bauxite factory in Henan Province, China. The lime was provided by Jiangxi Xinyu Huihui Industrial Co., Ltd. in Xinyu, China. Fly ash was selected from Henan Dingnuo Purification Materials Co., Ltd. in Henan Province, China with a fineness of 225 mesh and an ignition loss rate of 15.2%. The physical properties of silty sand and red mud were determined in this study using the test method for the physical properties of materials developed by Li et al. [20]. The basic physical properties of the silty soil and RM are shown in Table 1.

Table 1. Basic physical properties of test materials.

Physical Property	Materials	
	Silty Soil	**Red Mud (RM)**
Specific gravity	2.65	2.83
Plastic limit (%)	8.22	33.8
Liquid limit (%)	19.2	50.2
Optimum water content (%)	9.26	31.3
Maximum dry density ($g \cdot cm^{-3}$)	1.913	1.518
Loss-on-ignition (%)	/	14.67

Additionally, Table 2 lists the materials' chemical makeup and content. Table 2 shows that SiO_2, which makes up 67.89% of the oxides in silty soil, was the predominant oxide. The primary oxides present in RM were 20.1% SiO_2 and 32.02% CaO, respectively. The lime had the highest CaO content. The main oxides of the fly ash were SiO_2 and Al_2O_3, which indicates potential gelation activity [21].

Table 2. Main chemical compositions of test materials.

Chemical Compositions (%)	Materials			
	Silty Soil	**RM**	**Lime**	**Fly Ash**
Al_2O_3	9.58	20.1	/	36.3
SiO_2	67.89	13.28	/	42.6
Fe_2O_3	5.97	3.32	/	1.95
CaO	3.04	32.02	95.6	4.6
TiO_2	2.86	3.81	/	1.15
K_2O	1.75	0.35	/	0.52
MgO	2.82	1.16	0.96	/
Na_2O	/	10.9	/	/
SO_3	0.46	/	0.06	/
Others	5.63	15.06	3.38	12.88

Figure 2 shows the particle gradation curve. It can be seen from Figure 2 that the non-uniformity coefficient (C_u) of RM is less than 5, and the curvature coefficient (C_c) is less than 1. The powder particle content of RM reached 88.3%. The particle size distribution of RM was more uniform, indicating that its permeability is better. Silty soil exhibited a good particle gradation. Additionally, the sand grain content of the silty soil was 65.66%.

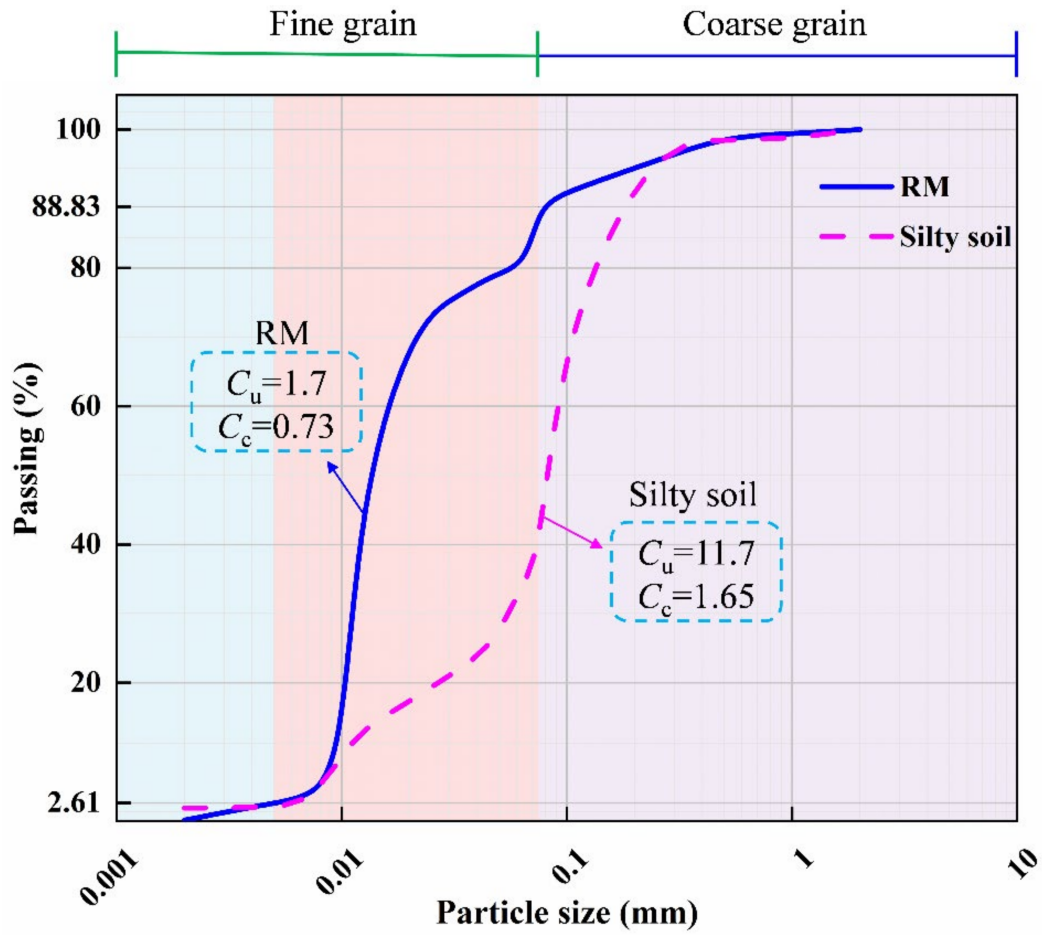


Figure 2. Gradation curve of RM and silty soil.

2.2. Test Methods

Table 3 lists the mechanical test scheme and microscopic test scheme. While ensuring that we used red mud as much as possible, we determined that the red mud content still fell below 30% [22,23]; the ratio of lime to fly ash in LF-RMS was 1:2. Before the test, the dry material was weighed and mixed well, and then mixed well again after the addition of water. In order to guarantee even distribution of the water, the mixtures were sealed in bags for 12 h. For ease of description, the specimen containing 10% LF and 17% RM is hereafter referred to as $D_{10\%LF+17\%RM}$.

Table 3. Mechanical test scheme and microscopic test scheme.

Tests	D_{RM} (%)	D_{LF} (%)	Curing Time (d)	Numbers
Mechanical test	17, 20, 23, 26	10, 20, 30	7, 28, 90	\
Microscopic test	26	20	28	LF-1
	23	10		LF-2
		20		LF-3
		30		LF-4
	23	20	90	LF-5

Before preparing the specimens, compaction tests [24] were performed on each material proportion of the soil. The maximum dry density and optimum moisture content of LF-RMS were obtained from the test results, as shown in Figure 3.

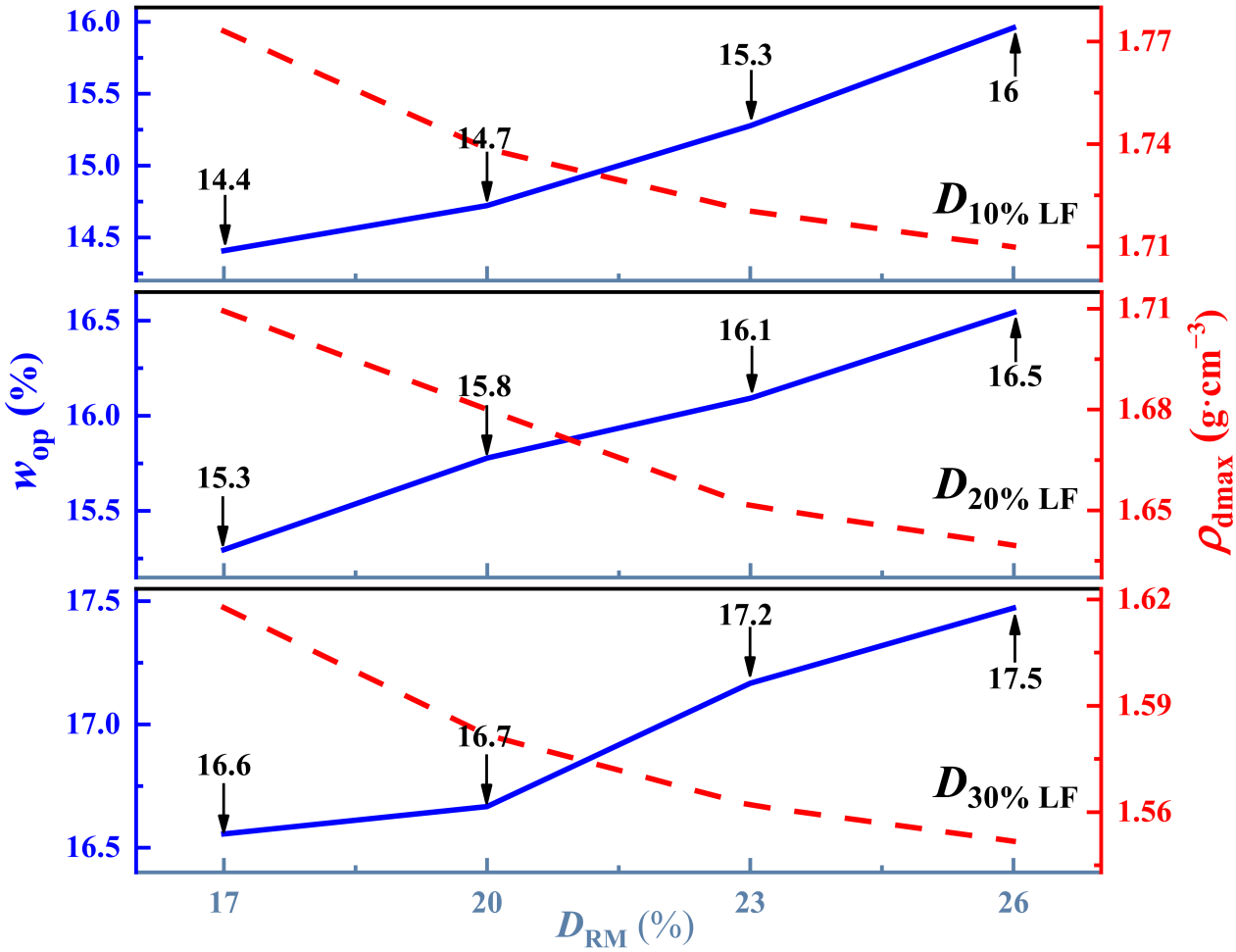


Figure 3. $\rho_{d\ max}$ and w_{op} curve of LF-RMS.

Detailed Tests

The UCS test involved the static pressure method, which was used to press cylindrical specimens with dimensions of 50 mm × 50 mm and a compaction degree of 95% [10]. Specimen preparation proceeded as follows:

(a) The mixture was compressed into three layers within the mold.
(b) After the specimen was demolded, it was wrapped in cling film and placed in a box with a consistent humidity level of 95% and a temperature of 20 °C.
(c) The specimens were submerged in water for twenty-four hours on the final day of curing.

A YYW-2 unconfined compressive strength tester was used during the unconfined compressive strength test, and the axial strain rate was controlled at 1 mm/min [25]. The preparation and maintenance of LF-RMS specimens are shown in Figure 4.

The instruments and parameters used in microscopic tests and component analysis experiments are presented in Table 4.

It is important to note that all water was removed from the surface of the specimens prior to UCS testing. Briefly, 15 mg of the treated specimens were weighed and placed inside an alumina crucible for the TG-DTG test. To ensure the SEM test specimens were fully dry and usable, they were sprayed with gold after being freeze-dried in liquid nitrogen.

The corrosion of LF-RMS was tested using the glass electrode method. To create the leachate, the specimen—which had a 10:1 liquid–solid ratio—was placed in an oscillator for 8 h and left there for 16 h before the test. The electrode was submerged in the specimen, and the pH value was determined.



Figure 4. Preparation and maintenance of LF-RMS specimens.

Table 4. Test Instruments and Parameters.

Test Names	Test Instruments	Test Parameters
XRD test	Bruker D8 Advance X-ray diffractometer (Germany)	2θ:5° to 80°; the scanning rate: 0.002 to 100°/min
TG-DTG test	STA499F5 synchronous thermal analyzer	The temperature range: 0 to 1000 °C; rising rate: 20 °C/min
SEM test	Ultra-high-resolution field-emission scanning electron microscope from Hitachi High-Tech SU8100 series	10,000× magnification

To determine the toxicity of heavy metal ion leaching in LF-RMS, the specimen (9.5 mm) was first dried, and then the leaching agent (sulfuric acid and nitric acid) was added in a 10:1 liquid–solid ratio. The leaching solution was diluted and filtered through a 0.22 μm membrane after shaking [26].

Using an FP-90041 low background multi-channel γ-ray spectrometric survey (which had an extended uncertainty of less than 15%, an energy resolution of less than 7%, and a measurable nuclide activity range of 10 Bq ~ 2000 Bq), the radioactivity level of LF-RMS was determined [27].

3. Results and Analysis

3.1. Strength Characteristics Analysis

3.1.1. Axial Stress–Strain Curve

The LF-RMS stress–strain curves, or σ-ε curves, are depicted in Figure 5. The σ-ε curves of LF-RMS with 7- and 28-day curing times exhibit an ambiguous peak point, a relatively delayed stress decline following the peak, and overall performance that exhibits plastic failure features. Due to the slow process of the volcanic ash reaction producing strength, LF-RMS had fewer early cementation products, which made the soil cementation strength weak. Furthermore, the volume expansion phenomenon occurred in the early stage of lime hydration, meaning it was more likely to cause weak connections between structural units and increased porosity in the soil, resulting in weakened soil strength. Therefore, when subjected to compressive stress, the deformation of the specimen was dominated by the sliding dislocation between soil particles and units. Additionally, the development of cracks was more uniform; there was no elastic deformation or concentration of stress caused by a sudden change in stress, thus indicating plastic deformation.

The specimens that were cured for ninety days showed an increase in the slope of the plastic deformation stage curve. The peak point was clearly visible, and the stress declined accordingly. The strain-softening characteristics of the specimen were enhanced;

this is because compared with the 7-day and 28-day specimens, the carbonation and crystallization reactions of lime in the 90-day specimens were more sufficient. Therefore, soil particles and the structural units were cemented with each other, resulting in enhanced structural strength. Under vertical load, soil underwent elastic deformation, and the cracks developed slowly and unevenly. Stress increased rapidly with strain and decreased rapidly after reaching a peak. Thus, the specimen shows brittle damage characteristics.

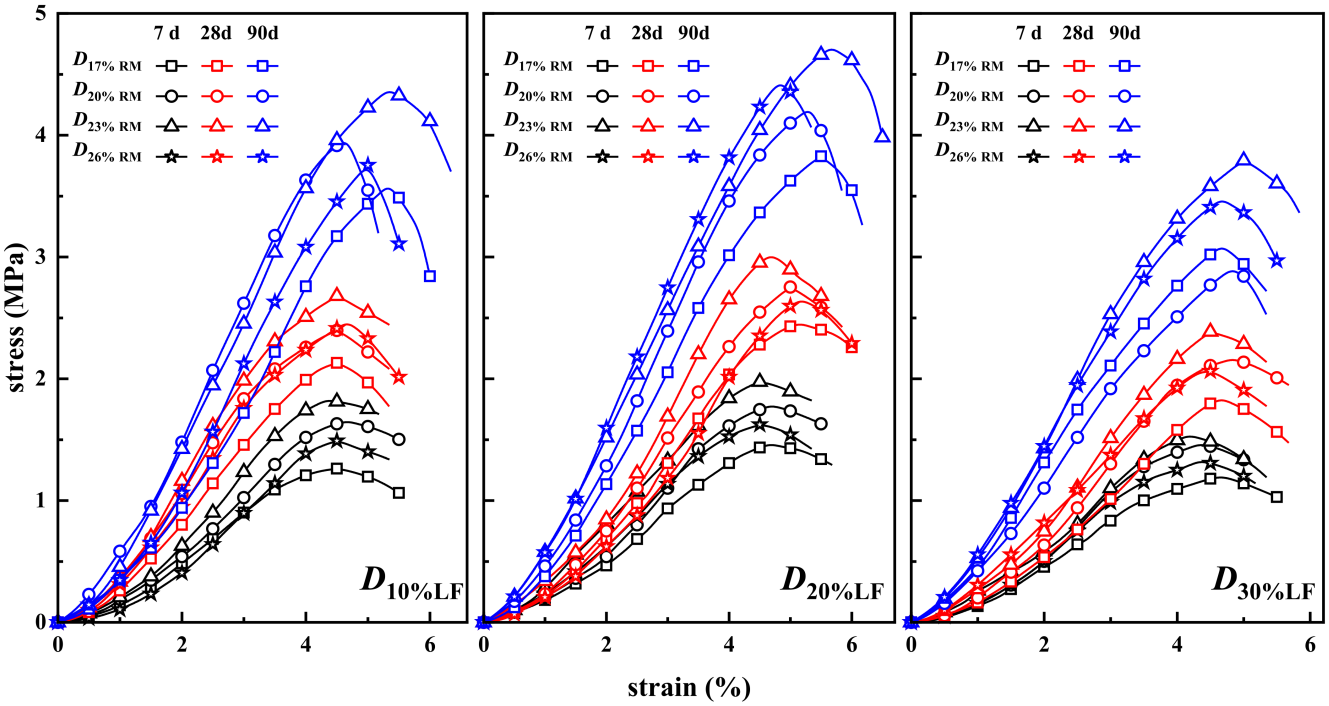


Figure 5. σ-ε curves of LF-RMS.

3.1.2. Compressive Strength

Figure 6 displays the LF-RMS' unconfined compression strength (UCS). Figure 6 illustrates that as D_{LF} rose, the UCS of LF-RMS first climbed and subsequently fell. When the red mud content was 17%, the compressive strength of the LF-RMS specimens increased to 1.26 MPa, 1.45 MPa, and 1.19 MPa, respectively, with increasing D_{LF} after 7 days of curing. The compressive strength of the specimen increased with the increase in curing time when the material contents remained constant. The compressive strength of $D_{10\%LF+17\%RM}$ cured for 7 days, 28 days, and 90 days was found to be 1.26 MPa, 2.13 MPa, and 3.59 MPa, respectively. The interaction of volcanic ash between LF and RM was primarily responsible for the materials' strength. The strength of the specimens decreased because there was less $Ca(OH)_2$ produced by the hydration of the lime in the $D_{10\%LF}$ specimens and fewer active ingredients (such as silica–alumina glass) in the fly ash. However, the strength of $D_{30\%LF}$ specimens decreased due to the heat released from the hydration reaction and increased cementitious material. First, the hydration process of lime released a large amount of heat, causing water to evaporate from the specimen. The reduction of water in the specimen inhibited the hydration reaction of lime and the dissolution of $Ca(OH)_2$, which reduced the rate at which cementation products formed. Second, the heat released from the lime hydration reaction also caused the particle aggregates to expand, resulting in the destruction of the soil structure. However, the moderate expansion of the particle aggregates caused by the hydration of lime in the $D_{20\%LF}$ specimens had the effect of compacting soil particles, making the soil structure more dens.

As the D_{RM} increased, the strength of the LF-RMS first increased and then decreased, and the UCS value of $D_{23\%RM}$ reached its maximum. When the lime–fly ash content was 10%, the strength of LF-RMS specimens cured for 7 days increased with D_{RM}, measuring

1.26 MPa, 1.65 MPa, 1.82 MPa and 1.49 MPa, respectively. When RM was added, an alkaline environment was created, which then increased the rate of dissociation of $Ca(OH)_2$ and the hydration of lime to form $Ca(OH)_2$. Such an environment also broke the silica–oxygen bonds and aluminum–oxygen bonds within active substances such as vitreous silica–aluminum in fly ash as well as increasing their activity. Therefore, the formation of more gel-like materials in the $D_{26\%RM}$ specimen led to a decrease in its UCS. Because RM particles encapsulated lime, they hindered the formation of calcium hydroxide and reduced the strength of the specimens.

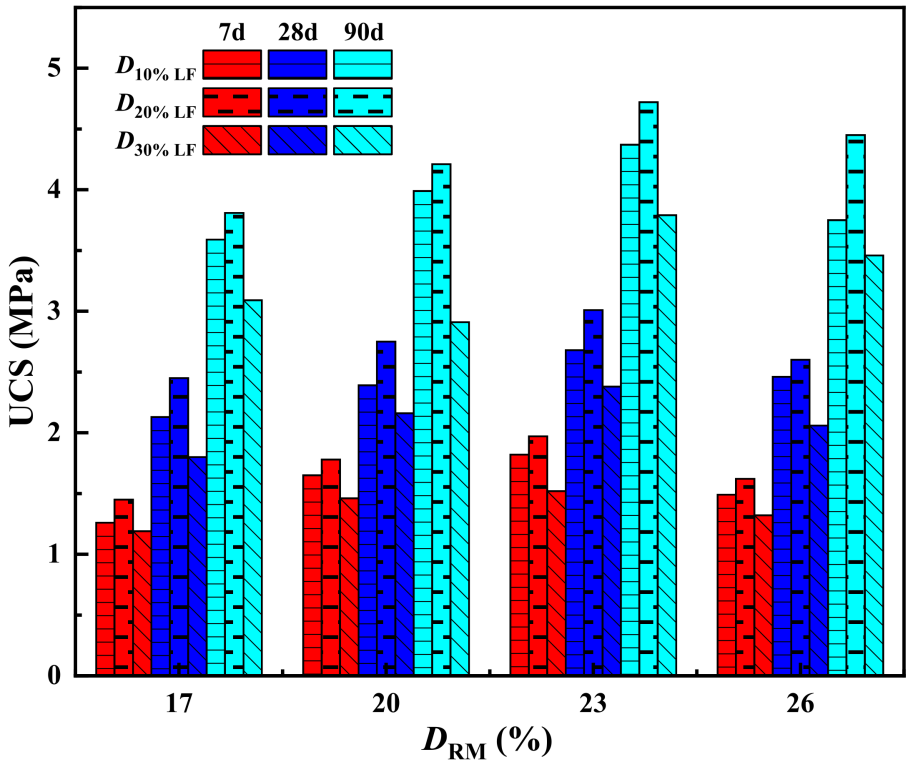


Figure 6. UCS of LF-RMS.

The primary cause of the 90-day strength of LF-RMS was the crystallization and carbonization of $Ca(OH)_2$, which proceeded in tandem with curing. Crystals of $Ca(OH)_2$ and $CaCO_3$ were produced when $Ca(OH)_2$ crystallized and became carbonated. The $Ca(OH)_2$ crystals connected with soil particles to form a crystalline network, thereby improving the structural strength of the specimen. $CaCO_3$ exhibited high cementation strength and water stability, which effectively increased the cementation strength of the soil.

We found optimal dosages of LF and RM for LF-RMS. The UCS of the $D_{20\%LF+23\%RM}$ specimen was the largest (UCS_{MAX} = 4.72 MPa), and its deformation resistance was relatively strong. When $D_{23\%RM}$ and D_{LF} were 10%, 20%, and 30%, the UCS of LF-RMS was 1.82 MPa, 1.97 MPa, and 1.52 MPa after 7 d, respectively. These results meet the "7-day unconfined compressive strength standard for lime and fly ash stabilized materials" [28] for highway subgrade strength lower limit requirements (>0.7 MPa). Therefore, for the application of LF-RMS in practical construction, an optimal mix ratio of $D_{20\%LF\,+\,23\%RM}$ was recommended.

3.1.3. Deformation Characteristic

The strain that corresponds to the specimen's maximal stress was known as the failure strain (ε_f). The greater the ε_f, the stronger the ductility. Figure 7 shows the variation curve of the LF-RMS' failure strain (ε_f) with D_{RM}. Figure 7 illustrates that among specimens with curing times of 7 and 28 days, the ε_f of $D_{23\%RM}$ was the lowest. Since the LF-RMS with $D_{23\%RM}$ contained more hydration products than the other specimens ($D_{17\%RM}$, $D_{20\%RM}$

and $D_{26\%RM}$), the specimens had a low ε_f and poor ductility. However, the specimens were not strong enough to resist damage under significant stress, thus exhibiting a strain-softening characteristic. Compared to other specimens with plastic deformation properties, the ε_f of $D_{23\%RM}$ occurred fastest. This was consistent with the stress–strain curve exhibited in Figure 4. As can be seen in Figure 7, the highest ε_f of $D_{23\%RM}$ occurred after 90 days of curing time. Furthermore, among all of the curing times, the ε_f of $D_{20\%LF}$ was the highest.

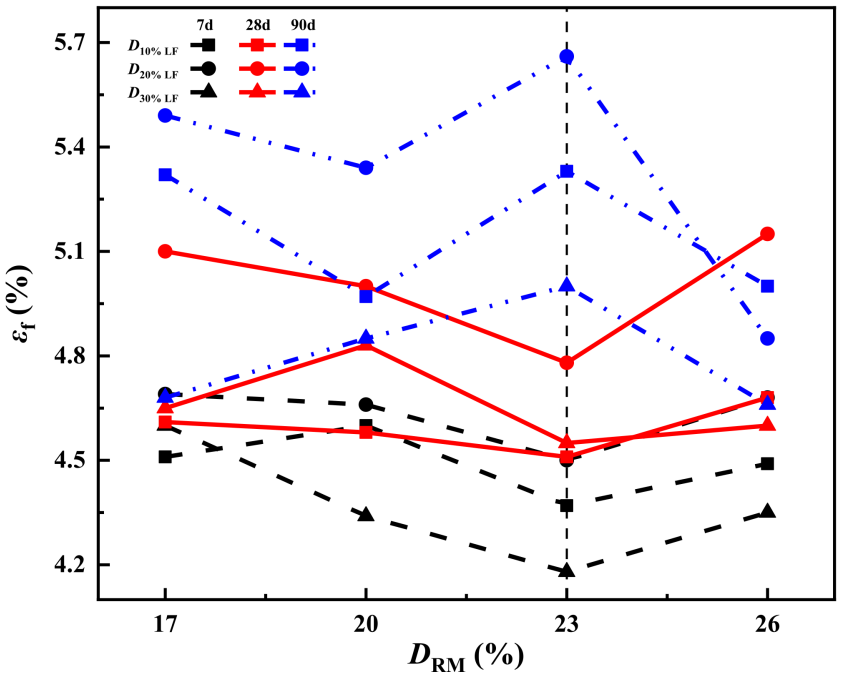


Figure 7. ε_f of LF-RMS.

The strength of a specimen's resistance to deformation was shown by the deformation coefficient (E_{50}), which was the secant modulus at the point on the σ-ε curve that corresponds to half of the failure strain. The strength of the deformation resistance increased with increasing E_{50} [29]. Figure 8 shows the variation curve of E_{50} with D_{RM}. The E_{50} value of $D_{20\%LF+23\%RM}$ was the largest, indicating that the $D_{20\%LF+23\%RM}$ specimen had the strongest resistance to deformation. Since the $D_{20\%LF+23\%RM}$ specimen produced the most cementitious products, the deformation resistance of the specimen was enhanced. Although the ε_f of the $D_{20\%LF+23\%RM}$ specimen was small in the initial stage, its ε_f grew fastest as the curing time increased. Overall, the LF-RMS deformation characteristics of $D_{20\%LF+23\%RM}$ were optimal.

Figure 9 shows the relationship between UCS and failure strain (ε_f), and deformation coefficient (E_{50}), where ε_f and E_{50} were positively related to UCS. The deformation characteristics also improve with increasing UCS. Figure 9a demonstrates that ε_f exhibits a generally rising trend with an increase in the UCS of LF-RMS, suggesting that LF-RMS had more strength and deformation resistance. A notable rise in E_{50} can be seen in Figure 9b, suggesting that the resistance of LF-RMS to deformation increased with its strength.

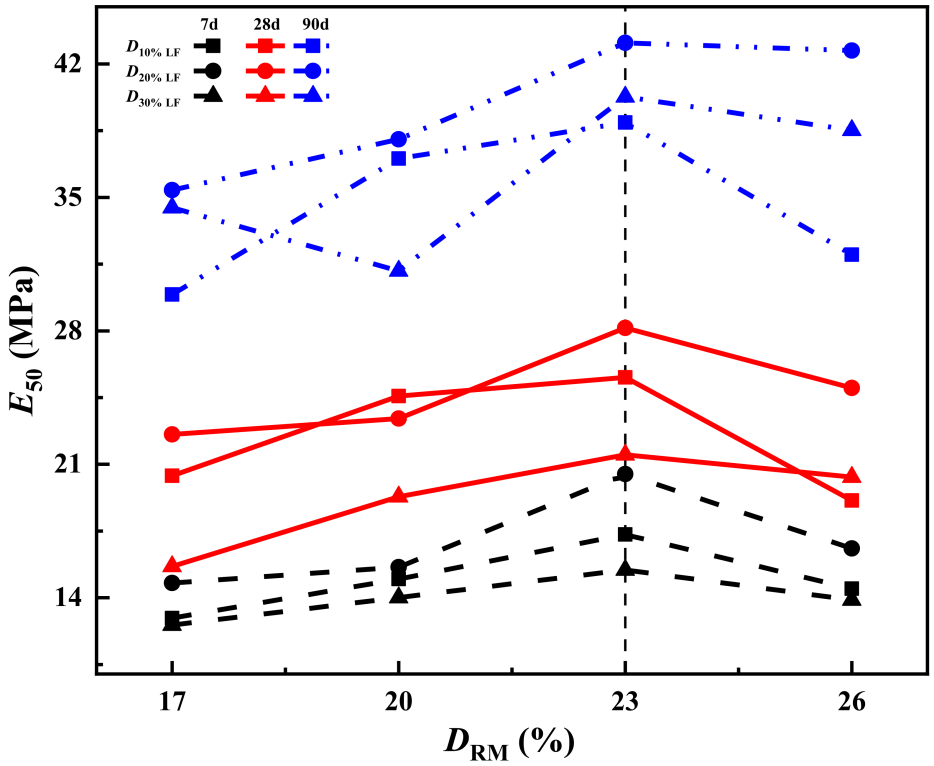


Figure 8. E_{50} of LF-RMS.

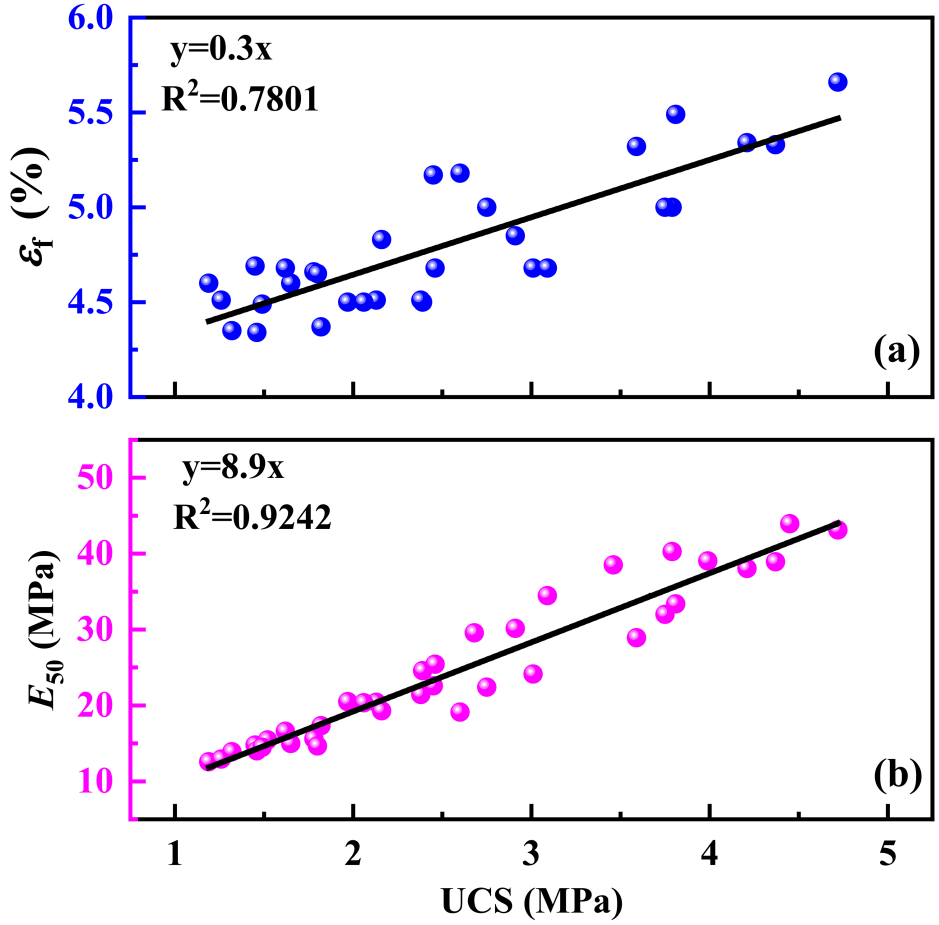


Figure 9. Relationship curves: (**a**) UCS and ε_f; (**b**) UCS and E_{50}.

3.1.4. Failure Characteristic

Photographs of typical failure characteristics upon UCS testing are shown in Figure 10. The failure modes of specimens were closely related to their strength characteristics. Figure 10 shows that the specimens with UCS values of 1.26 MPa, 2.13 MPa, and 1.97 MPa of $D_{10\%LF+17\%RM}$ (7 d, 28 d) and $D_{20\%LF+23\%RM}$ (7 d), respectively, exhibited tensile cracking damage. When the strength of the specimen was low, the hydration reaction produced fewer cementitious materials, resulting in the structure of the specimen being insufficiently dense. Vertical fractures initially occurred on the weak surfaces of the specimen as a result of horizontal tensile pressures applied to its perimeter due to compressive stress. As the stress continued to increase, longitudinal cracks gradually propagated, and the specimen appeared damaged (either totally or locally) by stress cracking. Because the process of specimen failure was slow, the specimen demonstrated plastic failure. As the specimen curing times or D_{RM} grew, more gel materials were produced by the hydration processes occurring inside the specimens. Such processes increased the strength of the specimen, and the specimen exhibited shear failure characteristics. For instance, the specimens of $D_{10\%LF+17\%RM}$ at 90 d and $D_{20\%LF+23\%RM}$ at 28 d and 90 d demonstrated shear failure, and their UCS values were 3.59 MPa, 3.01 MPa, and 4.72 MPa, respectively. The hydration process generated a greater volume of cementitious materials and intensified the connection between structures, resulting in enhanced overall structural integrity. Under the action of compressive stress, longitudinal cracks develop but do not affect the overall structural strength. With the further increase in stress, displacement occurred at the location of weakest cementation in the specimen, and then the oblique crack developed the shear failure of the surface.

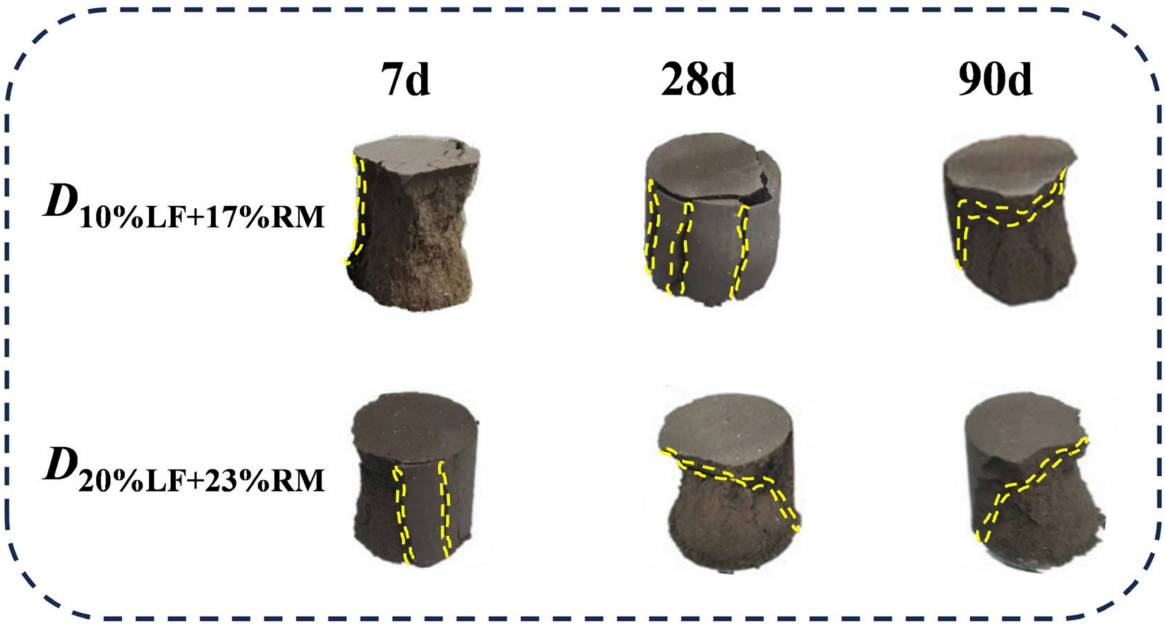


Figure 10. Typical failure pattern of LF-RMS.

3.2. Analysis of the Solidified Mechanisms of LF-RMS

3.2.1. X-ray Diffraction Analysis

Figure 11 shows the XRD pattern of LF-RMS, wherein it can be seen that the low active substances present in minimal proportions in LF-RMS were not only quartz and hematite but also mullite ($3Al_2O_3$) within fly ash. The hydration reaction of lime, the pozzolanic reaction with fly ash and RM, and the crystallization and carbonization processes were the primary sources of its strength. These reactions caused the soil to form a cementitious and crystalline structure, enhancing its structural strength. $Ca(OH)_2$, calcium silicate hydrate (C-S-H), calcium aluminate hydrate (CAH), and $CaCO_3$ were the principal hydration products

of LF-RMS. The hydration reaction of lime produced a large amount of $Ca(OH)_2$, which has low solubility. After $Ca(OH)_2$ reached saturation, it interacted directly with OH^-, Ca^{2+}, and O^{2-} to form $Ca(OH)_2$. Some $Ca(OH)_2$ gradually formed $Ca(OH)_2$ crystal ($Ca(OH)_2 \cdot nH_2O$) after absorbing water, and some reacted with CO_2 in water to form $CaCO_3$ crystals (i.e., the crystallization and carbonization reactions of lime). The slow reaction process contributed to the long-term strength of LF-RMS [30]. The reaction produced crystals with high strength and strong water stability. The main reactions' equations are shown in (1)–(3).

$$CaO + H_2O \rightarrow Ca(OH)_2 \quad (1)$$

$$Ca(OH)_2 + nH_2O \rightarrow Ca(OH)_2 \cdot nH_2O \quad (2)$$

$$Ca(OH)_2 + CO_2 + nH_2O \rightarrow CaCO_3 + (n + 1)H_2O \quad (3)$$

In the early stages of strength formation, most of the $Ca(OH)_2$ dissolved in water. The dissociated Ca^{2+} and OH^- reacted with the silica–alumina active substances released from both fly ash and RM to produce gelling products (e.g., C-S-H and C-A-H) [31,32]. This process is the volcanic ash reaction, which is the main reason for the strength of LF-RMS. Under the action of alkali excitation, the silicon–aluminum glass in fly ash accelerated the fracturing and generated cementitious products. These products gradually condensed and hardened, which improved the strength of LF-RMS. However, the water content of the soil increased at $D_{26\%RM}$, which was not conducive to the transformation of the cementitious structure of lime into a crystalline structure. It also hindered the dispersion of lime particles into finer particles, and it was difficult for OH^- to react directly with the CaO in lime accordingly to further generate $Ca(OH)_2$. Thus, the structural strength of the soil was reduced.

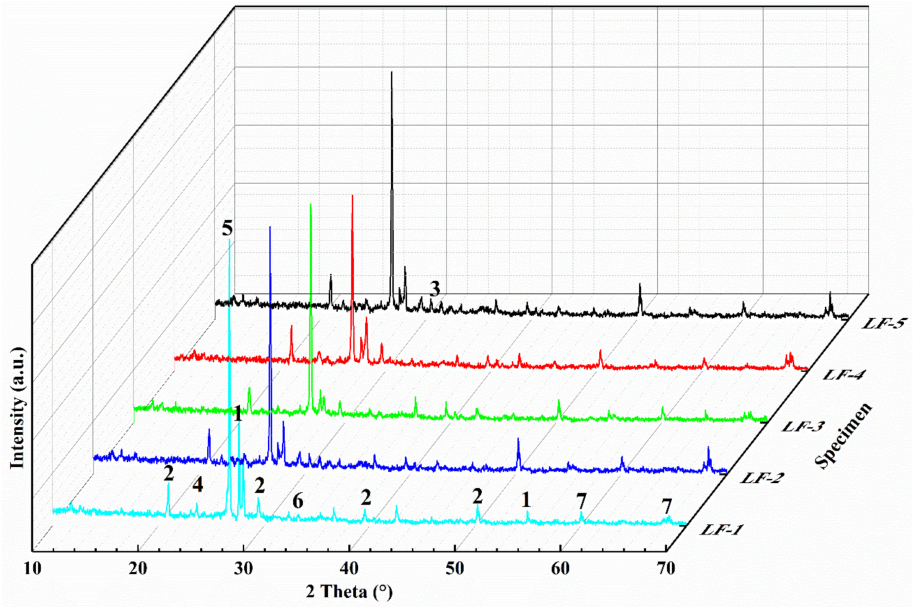


Figure 11. XRD pattern of LF-RM (1. $Ca(OH)_2$; 2. Calcium Silicate Hydrate (C-S-H); 3. $CaCO_3$; 4. mullite ($3Al_2O_3 \cdot 2SiO_2$); 5. quartz (SiO_2); 6. hematite (Fe_2O_3); 7. Calcium aluminate hydrate (C-A-H)).

3.2.2. Thermogravimetric–Differential Thermal Analysis

Figure 12 illustrates the TG-DTG results of LF-RMS, and Table 3 displays the corresponding specimen numbers. As the temperature rose, the mass loss rate of LF-RMS could be divided into four phases, as shown in Figure 12.

During stage I, which occurred at temperatures below 120 °C, the mass loss in soil could primarily be attributed to the elimination of free water. The mass loss rates ranged from a maximum of 1.36% (LF-2) to a minimum of 0.68% (LF-4). It can be seen by LF-4 that

D_{LF} had a large effect on the water content of the LF-RMS. As a large amount of heat was released when the hydration reaction occurred with too much lime in LF, the soil lost water, which was unfavorable for the subsequent hydration reaction.

During stage II (120–700 °C), mass loss occurred as a result of the elimination of bound water from the hydration products and certain minerals. At this point, the mass loss rate indicated the amount of hydration products present. The maximal mass loss rate in stage II was 4.31% (LF-5). The specimens' hydration products progressively rose as the curing time increased. A comparison of LF-2, LF-3, and LF-4 revealed that LF-3 reacted most fully, resulting in the most gelling products at the same D_{RM}. The maximum mass loss was 4.02% (LF-3). LF-4 had the smallest mass loss rate of 3.40%. At this time, the hydration products were minimal, and the specimen strength was the lowest, which was consistent with the macroscopic test results. The release of heat from the hydration reaction and volume expansion caused the number of gelling products to decrease when D_{LF} was excessive. Comparing LF-1 and LF-3, it was found that the mass loss rate of LF-1 was lower than that of LF-3, indicating that the hydration products of LF-1 were less, resulting in a lower strength than that of LF-3. This phenomenon is due to the inhibition of $Ca(OH)_2$ production and its subsequent crystallization reaction due to the high alkalinity and the high number of RM particles. Therefore, if the optimal dosage of D_{RM} is exceeded, the hydration reaction of LF-RMS is adversely affected.

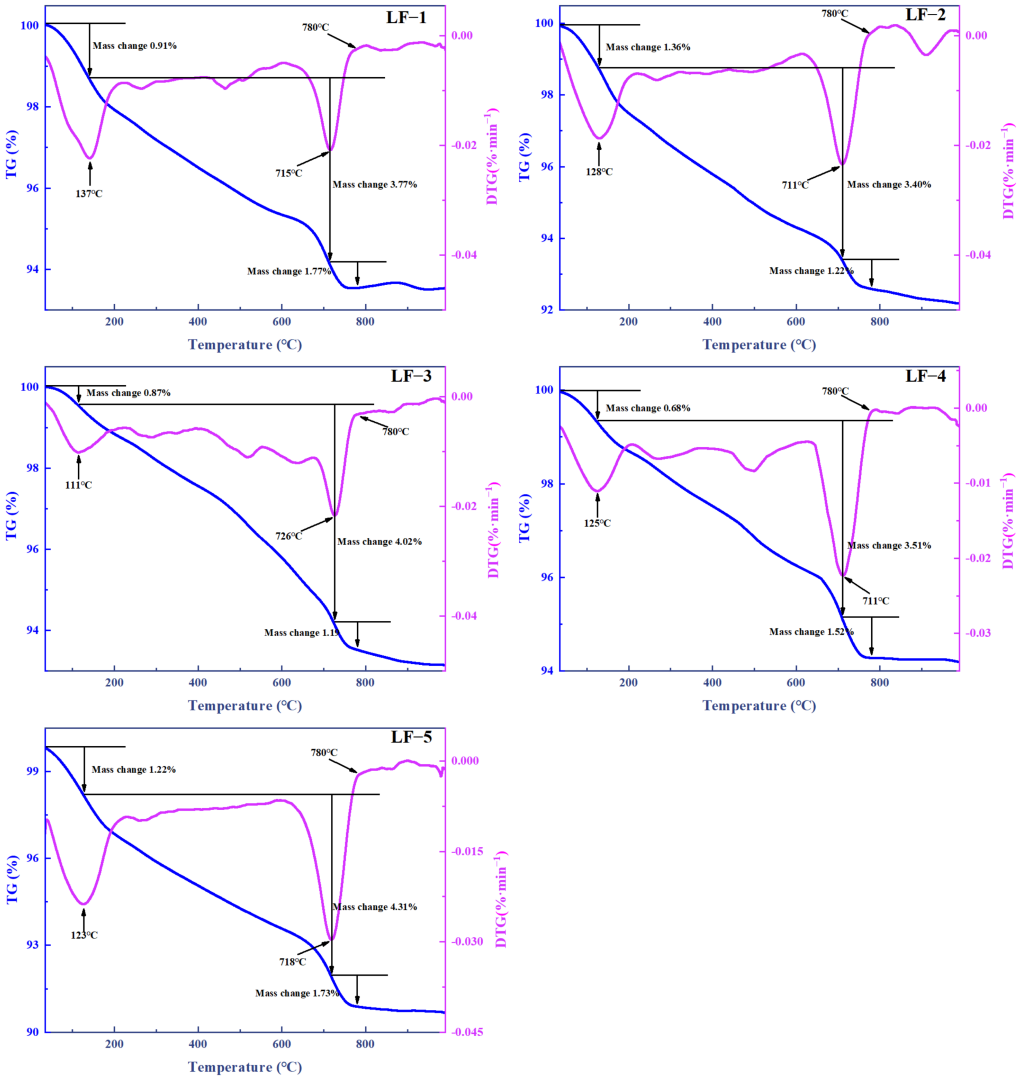


Figure 12. TG-DGT of LF-RMS.

The loss of mass during stage III (700–780 °C) is primarily attributable to the decomposition of $Ca(OH)_2$ crystals and $CaCO_3$ crystals. The maximum mass loss in this phase was 1.73% (LF-5). It can be seen by LF-5 that a large number of $Ca(OH)_2$ and $CaCO_3$ crystals were formed due to the crystallization and carbonization of lime, which significantly improved the strength of LF-RMS after 90 days. The rate of mass loss during stage III at 28 d reflected the degree to which the specimen was hydrated: the smaller the mass loss of the specimen, the fewer the $Ca(OH)_2$ crystals that were present (i.e., the more adequate the hydration reaction). The TG curve of LF-3 shows that LF-3 had the smallest mass loss (1.19%), whereas LF-4 had the largest mass loss (1.52%). Furthermore, the consumption of $Ca(OH)_2$ was greatest in LF-4, and the hydration reaction produced the most cementitious materials. Continued increase in either D_{RM} or D_{LF} affected the LF-RMS hydration reaction, resulting in a decrease in specimen strength.

Phase IV (above 780 °C) showed the destruction and decomposition of some inert materials and mineral structures in RM and fly ash.

3.2.3. Scanning Electron Microscopy

Figure 13 shows SEM images of LF-RMS at 10,000× magnification. At D_{LF} = 10% (Figure 13a), LF-RMS hydration generated insufficient gelling material due to the smaller proportion of LF. Most of said material took the form of strips and flakes, the surface area and cementation ability of which were limited.

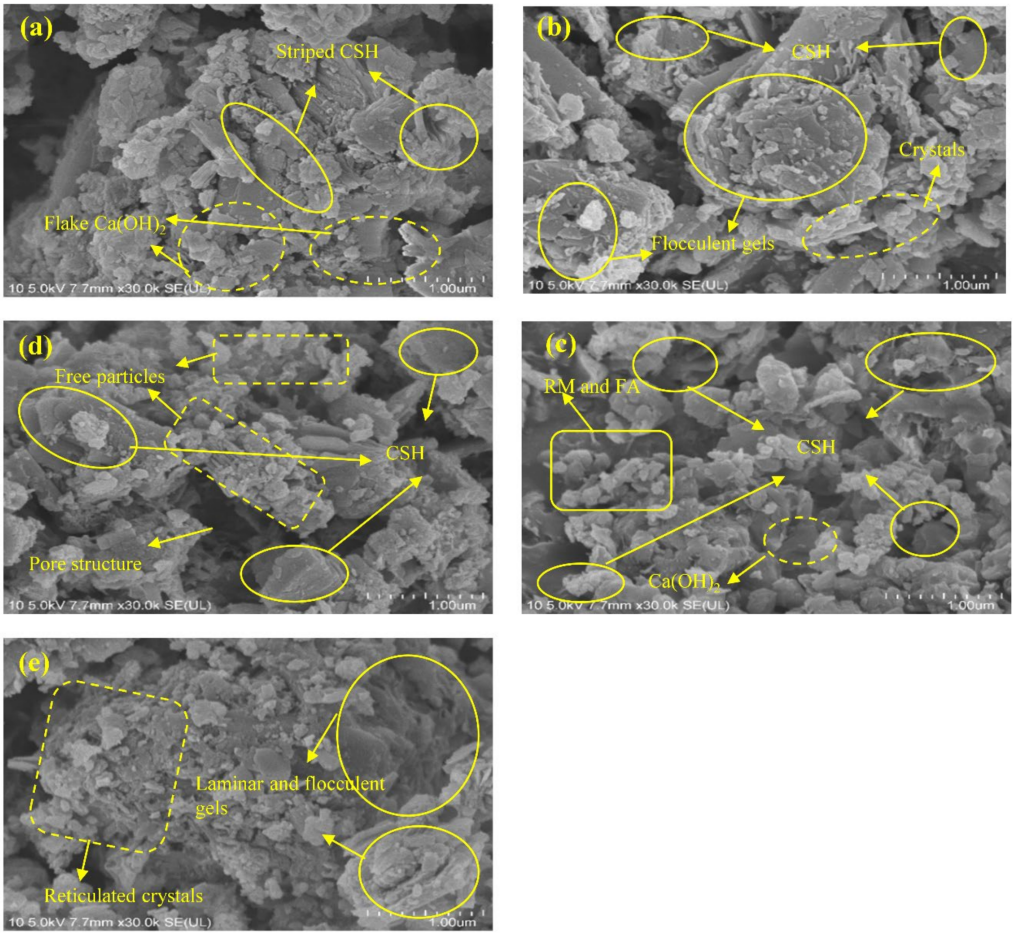


Figure 13. SEM images of LF-RMS: (**a**) $D_{10\%LF+23\%RM}$ (28 d); (**b**) $D_{20\%LF+23\%RM}$ (28 d); (**c**) $D_{30\%LF+23\%RM}$ (28 d); (**d**) $D_{20\%LF+26\%RM}$ (28 d); (**e**) $D_{20\%LF+23\%RM}$ (90 d).

The gels were distributed side by side with a small amount of lamellar $Ca(OH)_2$, which could not effectively fill the pores, making it difficult to form a dense structure.

From Figure 13b,e, it can be seen that the $D_{20\%LF+23\%RM}$ specimen had the highest overall compactness. Gelling products such as C-S-H in the soil were flaky and flocculent; their surface area was large, and the pores of the soil were densely filled. $Ca(OH)_2$ crystals and $CaCO_3$ crystals were also present in the soil. $Ca(OH)_2$, $CaCO_3$ crystals, and gelling products were interspersed or intertwined to form a complete and strong skeletal structure. Although there were some unhydrated RM and fly ash particles in the soil, they were tightly adsorbed around the cementation products to form a stable structure. The $D_{30\%LF+23\%RM}$ specimen at 28 d had the loosest microstructure (Figure 13c). Layered and flaky C-S-H gels can be observed in Figure 13c. However, due to the release of heat and the volume expansion caused by lime hydration, the distribution of cementation products in the loose structural system was messy. Therefore, it was difficult for the soil to form a complete structure. Moreover, the process of releasing heat from hydration consumed water and inhibited the decomposition of $Ca(OH)_2$, resulting in an insufficient hydration reaction. In other words, there were fewer cementitious products, and more RM and fly ash particles without hydration reaction. In addition, more $Ca(OH)_2$ crystals were present in LF-RMS because the decomposition of $Ca(OH)_2$ was inhibited. This phenomenon aligns with the findings of our thermogravimetric analysis. It was difficult for the crystals to develop into a tightly structured crystalline network due to the loose structure of the soil. Various lamellar and lamellar gelling products are present in Figure 13d. There are many RM particles in the $D_{26\%RM}$ specimen that did not undergo a hydration reaction. Large cementation structures are difficult for gelling products like C-S-H to develop because of the impact of free RM particles on structural density. Moreover, lime particles are enveloped by RM particles, which reduces the number of $Ca(OH)_2$ hydration products, making the void structure larger and limiting the overall compactness.

3.3. Environmental Impact Analysis

Red mud was a solid waste with high alkalinity and has been found to contain radioactive substances. The chemical properties of quicklime and fly ash are alkaline. Additionally, fly ash contains some harmful substances (e.g., cadmium, mercury, lead, chromium, and arsenic) and radioactive elements (e.g., uranium, thorium, and potassium) [33,34]. Therefore, the environmental impact of LF-RMS s needs greater consideration when this material is to be used for subgrade filling. According to the mechanical testing, the optimal dosage ($D_{20\%LF+23\%RM}$ specimen cured for 28 days) was selected for environmental index testing. Table 4 presents the radioactivity and corrosivity of RM and LF-RMS. The internal irradiation index (I_{Ra}) and external irradiation index (I_γ) were also calculated [35]. Compared with RM, the I_{Ra} and I_γ of LF-RMS decreased by 1.63 and 1.69, respectively. Moreover, the corrosiveness of LF-RMS was also reduced when compared with the pH values of RM and LF-RMS in Table 5. The pH of LF-RMS was 9.87, which was 1.84 lower than that of RM.

Table 5. Presents the radioactivity and corrosivity of LF-RMS.

Materials	Radioactive Specific Activity ($Bq \cdot kg^{-1}$)			Corrosiveness
	^{226}Ra	^{232}Th	K40	PH
RM	508	265	1050	11.71
LF-RMS	118	97	332	9.87

Figure 14 illustrates a comparison of toxic leaching concentrations of RM and LF-RMS. It can be seen from Figure 14 that the toxic leaching concentrations of RM and LF-RMS were lower than normative limits [36]. The leaching concentration of fluoride decreased by 43.3%, while the leaching concentration of barium metal decreased by 97.2%. As a whole, LF-RMS reduced more than 60% of the heavy metal leaching concentration. Because heavy metal ions were solidified by precipitation, adsorption, encapsulation, and replacement during the generation of gelling substances, the metal leaching concentration of LF-RMS could be reduced [37]. LF-RMS underwent hydration to form $Ca(OH)_2$ and C-S-H, and

a large amount of free Ca^{2+}, OH^-, and hydroxides were produced in the soil during this process. In an alkaline environment, heavy metal ions form hydroxide precipitates and calcium-containing complexes with these free hydration products [38]. The $Ca(OH)_2$ and $Al(OH)_3$ generated by the hydration reaction had the effect of adsorbing and encapsulating heavy metal ions. In summary, the solidification of heavy metal ions in LF-RMS was closely related to the rate at which cementitious materials are formed, and hydration products play a key role in the process of heavy metal solidification. Finally, an alkaline environment is conducive to the precipitation and replacement of heavy metals [39,40].

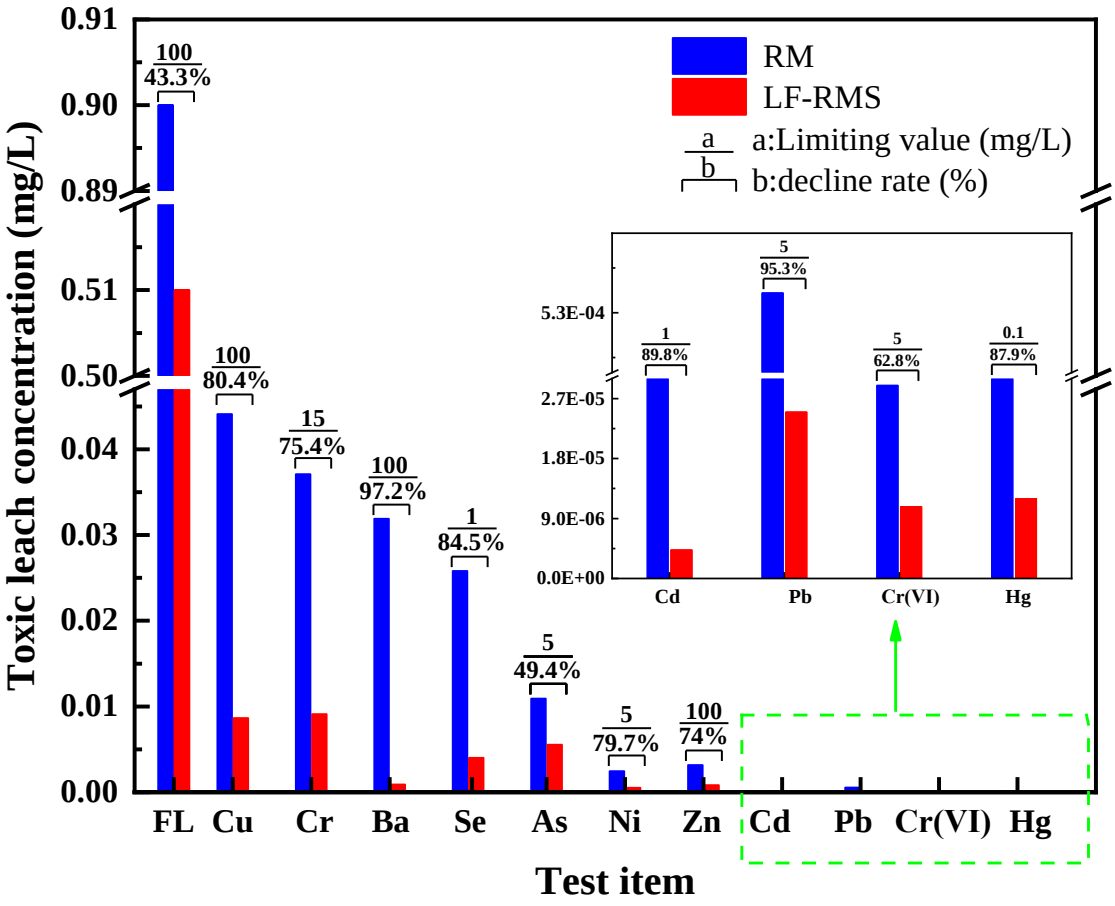


Figure 14. Reduction of toxic leach concentration.

4. Conclusions

In this study, an unconfined compressive strength test (USC test), scanning electron microscopy test (SEM), X-ray diffraction (XRD), thermogravimetric differential thermal analysis (TG-DTG), and environmental indices testing were carried out. The strength characteristics of lime–red mud-modified silty sand (LF-RMS) featuring different red mud and lime–fly ash ratios were studied, and the optimal ratio of LF-RMS was thereby determined. The mechanisms forming the strength of LF-RMS and changes in various environmental indicators were analyzed. The following conclusions could be drawn:

1. The peak value of the stress–strain curve after 90 days of curing was more significant than that at 7 and 28 days, and the stress decreased rapidly after reaching its peak value. The LF-RMS after 90 days of curing indicated brittle failure, and the specimens after 7 days and 28 days of curing indicated plastic failure. The deformation coefficient of the $D_{20\%LF+23\%RM}$ specimen was the largest with all curing times, suggesting that its ability to resist deformation was the strongest. The deformation coefficients for 7, 28, and 90 days of maintenance were 20.49, 28.15, and 43.11, respectively. The failure strain after 7 days and 28 days of curing was small, but the failure strain after 90 days

of curing time increased the most rapidly, indicating that the specimen exhibited the greatest ductility after 90 days.

2. The unconfined compressive strength of LF-RMS initially increased and then decreased with varying D_{LF} or D_{RM} values but identical curing times. When D_{LF} was a variable, the specimen containing 20% lime–fly ash exhibited the highest strength, while when D_{RM} was a variable, the specimen with 23% red mud demonstrated the greatest strength. Therefore, $D_{20\%LF+23\%RM}$ represented the optimal ratio of LF-RMS. In addition, strength increased with an increase in curing time. The strength values of the specimens cured for 28 d and 90 d with $D_{20\%LF+23\%RM}$ were 3.01 MPa and 4.72 MPa, respectively.
3. The LF-RMS hydration reaction of $D_{20\%LF+23\%RM}$ produced the most hydrated products and the densest structure. When D_{RM} or D_{LF} were too high, the decomposition of $Ca(OH)_2$ was inhibited, and the hydration reaction produced less gelling material. At this time, the soil structure was loose, and it was difficult for $Ca(OH)_2$ crystals to develop into a tightly structured crystalline network, which therefore decreased the strength of the soil.
4. The environmental impact of LF-RMS was greatly improved compared to pure RM. The overall concentration of heavy metals in LF-RMS decreased by more than 60%. The hydration products and crystallization in the LF-RMS played a key role in the solidification of heavy metal ions.

In conclusion, the strength of LF-RMS met the criteria of material specifications for road base filling. Despite the alkaline and radioactive nature of the red mud, the environmental parameters of LF-RMS remained within the standard range. According to the strength characteristics of LF-RMS, it may be used for base filling within highway structures. LF-RMS represents a novel solution to the problem of red mud stockpiling. The utilization of red mud as a road construction material not only necessitates the consumption of significant quantities of red mud but also reduces reliance on cement. Such a mixed material is currently utilized for road bases in natural environments, with no consideration given to road conditions in harsh environments. Its applicability is currently limited to roads in the Henan region. Therefore, it is recommended that future studies assess the strength and environmental characteristics of this material under harsh conditions and reveal its practical engineering applications in other regions.

Author Contributions: Conceptualization, Y.W.; Validation, X.L. and Y.W.; Formal analysis, S.Y., P.Y., X.Z., Y.S. and C.C.; Investigation, S.Y., P.Y., X.Z., Y.S. and C.C.; Data curation, S.Y. and X.L.; Writing—original draft, S.Y.; Writing—review & editing, P.Y. and X.L.; Supervision, X.L. and Y.W. All authors have read and agreed to the published version of the manuscript.

Funding: The authors gratefully thank the financial support of the National Natural Science Foundation of China (No. 51709290, Song Yin), the Key scientific research project plan of colleges and universities Scientific Research Project Plan of Colleges and Universities in Henan Province, China (grant number 20zx009, Yuzhou Sun), the Young Key Teachers in Colleges and Universities of Henan Province (No. 2020GGJS136, Song Yin), and the strength improvement plan of the advantageous disciplines of Zhongyuan University of Technology (No. GG202218, Song Yin).

Data Availability Statement: All of the data that support the findings of the study are available from the corresponding author on reasonable request.

Conflicts of Interest: The authors declare no conflict of interest.

References

1. Cui, W.; Liu, J.; He, G.; Duan, W.; Li, X.; Dong, X. Evaluation of active silica-alumina content and reactivity in bayer process red mud. *Constr. Build. Mater.* **2024**, *418*, 135502. [CrossRef]
2. Al-Fakih, A.; Nor, Z.M.; Basha, S.I.; Shaikh, M.N.; Ahmad, S.; Al-Osta, M.A.; Aziz, A. Characterization and Applications of Red Mud, an Aluminum Industry Waste Material, in the Construction and Building Industries, as well as Catalysis. *Chem. Rec.* **2023**, *23*, e202300039. [CrossRef]

3. Mukiza, E.; Zhang, L.; Liu, X.; Zhang, N. Utilization of red mud in road base and subgrade materials: A review. *Resour. Conserv. Recycl.* **2019**, *141*, 187–199. [CrossRef]
4. Feng, L.; Yao, W.; Zheng, K.; Cui, N.; Xie, N. Synergistically Using Bauxite Residue (Red Mud) and Other Solid Wastes to Manufacture Eco-Friendly Cementitious Materials. *Buildings* **2022**, *12*, 117. [CrossRef]
5. Qaidi, S.M.; Tayeh, B.A.; Isleem, H.F.; de Azevedo, A.R.; Ahmed, H.U.; Emad, W. Sustainable utilization of red mud waste (bauxite residue) and slag for the production of geopolymer composites: A review. *Case Stud. Constr. Mater.* **2022**, *16*, e00994. [CrossRef]
6. Khairul, M.; Zanganeh, J.; Moghtaderi, B. The composition, recycling and utilisation of Bayer red mud. *Resour. Conserv. Recycl.* **2018**, *141*, 483–498. [CrossRef]
7. Ai, T.; Zhong, D.; Zhang, Y.; Zong, J.; Yan, X.; Niu, Y. The Effect of Red Mud Content on the Compressive Strength of Geopolymers under Different Curing Systems. *Buildings* **2021**, *11*, 298. [CrossRef]
8. Zhang, J.; Gao, Y.; Li, Z.; Wang, C. Pb2+ and Cr3+ immobilization efficiency and mechanism in red-mud-based geopolymer grouts. *Chemosphere* **2023**, *321*, 138129. [CrossRef]
9. Cong, T.D.; Phuong, T.; Vu, M.T.; Nguyen, T.H. Effect of Calcium Hydroxide on Compressive Strength and Microstructure of Geopolymer Containing Admixture of Kaolin, Fly Ash, and Red Mud. *Appl. Sci.* **2023**, *13*, 5034. [CrossRef]
10. Salih, W.; Yu, W.; Dong, X.; Hao, W. Study on stress-strain-resistivity and microscopic mechanism of red mud waste modified by desulphurization gypsum-fly ash under drying-wetting cycles. *Constr. Build. Mater.* **2020**, *249*, 118772. [CrossRef]
11. Barmade, S.; Patel, S.; Dhamaniya, A. Laboratory and Field Evaluation of Stabilized Fly Ash as an Alternative Material for Sustainable Pavements. *J. Hazardous, Toxic, Radioact. Waste* **2022**, *26*, 04022028. [CrossRef]
12. Kumar, S.S.; Maheswaran, S. Thermal, Microstructural, and Mechanical Properties of Ternary Blended Geopolymers. *ACI Mater. J.* **2022**, *119*, 103–116.
13. Ou, X.; Zeng, Y.; Jiang, J.; Lyu, Z.; Chen, H.; Chen, G. Experimental Research on the Properties of Foamed Mixture Lightweight Soil with Red Mud. *Case Stud. Constr. Mater.* **2022**, *17*, e01673. [CrossRef]
14. Shi, J.; Liu, Y.; Li, Z.; Lei, J.; Yin, K.; Zhang, Z.; Xie, N. Upcycling use of red mud-based solid waste in engineered cementitious composites: Properties, activation mechanism, and life-cycle assessment. *J. Clean. Prod.* **2024**, *447*, 141504. [CrossRef]
15. Ke, G.; Zheyu, L.; Haishun, J. Study on long-term solidification of all-solid waste cementitious materials based on circulating fluidized bed fly ash, red mud, carbide slag, and fly ash. *Constr. Build. Mater.* **2024**, *427*, 136284. [CrossRef]
16. Ma, Q.; Duan, W.; Liu, X.; Fang, P.; Chen, R.; Wang, T.; Hao, Z. Engineering Performance Evaluation of Recycled Red Mud Stabilized Loessial Silt as a Sustainable Subgrade Material. *Materials* **2022**, *15*, 3391. [CrossRef] [PubMed]
17. Chandra, S.; Sahile, K. Utilization of Red Mud-Fly Ash Reinforced with Cement in Road Construction Applications. *Adv. Mater. Sci. Eng.* **2021**, *2021*.
18. Chandra, K.S.; Krishnaiah, S.; Reddy, N.G.; Hossiney, N.; Peng, L. Strength Development of Geopolymer Composites Made from Red Mud-Fly Ash as a Subgrade Material in Road Construction. *J. Hazard. Toxic Radioact. Waste* **2021**, *25*, 04020068. [CrossRef]
19. Liu, S.; Li, Z.; Li, Y.; Cao, W. Strength properties of Bayer red mud stabilized by lime-fly ash using orthogonal experiments. *Constr. Build. Mater.* **2018**, *166*, 554–563. [CrossRef]
20. Li, X.; Liang, Z.; Ren, K.; Yin, S.; Sun, Y. The Effect of Hydraulic History on Shear Strength of Silt. *Int. J. Geomech.* **2023**, *23*, 04023137. [CrossRef]
21. Long, Q.; Zhao, Y.; Zhang, B.; Yang, H.; Luo, Z.; Li, Z.; Zhang, G.; Liu, K. Interfacial Behavior of Slag, Fly Ash, and Red Mud-Based Geopolymer Mortar with Concrete Substrate: Mechanical Properties and Microstructure. *Buildings* **2024**, *14*, 652. [CrossRef]
22. Kumar, A.; Kumar, S. Development of paving blocks from synergistic use of red mud and fly ash using geopolymerization. *Constr. Build. Mater.* **2013**, *38*, 865–871. [CrossRef]
23. He, J.; Guo, T.; Li, Z.; Gao, Y.; Zhang, J. Hydration mechanism of red mud-fly ash based geopolymer. *Mater. Chem. Phys.* **2024**, *314*, 128807. [CrossRef]
24. *ASTMD698-12*; Standard Test Methods for Laboratory Compaction Characteristics of Soil Using Standard Effort. USA ASTM International: West Conshohocken, PA, USA, 2021.
25. Ma, K.; Liu, J.; Jiang, C.H.; Ma, X.F.; Huang, L.H.; He, C.Z.; Qi, C.Q. Compressive and tensile strength of polymer-based fiber composite sand. *J. Cent. South Univ.* **2022**, *29*, 528–545. [CrossRef]
26. Bai, Y.; Guo, W.; Zhang, Y.; Xue, C.; Xu, Z.; Gao, Q.; Xiao, C.; Zhao, Q. Low carbon binder preparation from slag-red mud activated by MSWI fly ash-carbide slag: Hydration characteristics and heavy metals' solidification behavior. *J. Clean. Prod.* **2022**, *374*, 134007. [CrossRef]
27. Li, X.; Yan, P.; Yin, S.; Zhang, X.; Liu, P.; Wang, Y. Strength Characteristics and Micro-Mechanism of Silty Soil Modified by Red Mud Co-Cement. *Sustainability* **2023**, *15*, 8762. [CrossRef]
28. *JTG/TF20-2015*; Technical Specification for Highway Pavement Base Construction. Beijing Ministry of Transport of the People's Republic of China: Beijing, China, 2015.
29. He, J.; Wang, X.Q.; Shi, X.K.; Li, Z.X. Unconfined Compressive Strength and Microscopic Characteristics of Soft Soil Solidified with Soda Residue and Ground Granulated Blast Furnace Slag. *J. Basic Sci. Eng.* **2021**, *29*, 376–386.
30. Saing, Z.; Samang, L.; Harianto, T.; Palanduk, J. Bearing capacity characteristic of subgrade layer quicklime treated laterite soil. *MATEC Web Conf.* **2018**, *181*, 11001. [CrossRef]

31. Elyasigorji, F.; Farajiani, F.; Manjili, M.H.; Lin, Q.; Elyasigorji, S.; Farhangi, V.; Tabatabai, H. Comprehensive Review of Direct and Indirect Pozzolanic Reactivity Testing Methods. *Buildings* **2023**, *13*, 2789. [CrossRef]
32. Hu, W.; Nie, Q.; Huang, B.; Shu, X.; He, Q. Mechanical and Microstructural Characterization of Geopolymers Derived from Red Mud and Fly Ashes. *J. Clean. Prod.* **2018**, *186*, 799–806. [CrossRef]
33. Li, W.; Wang, W.; Wu, D.; Yang, S.; Fang, H.; Sun, S. Mechanochemical treatment with red mud added for heavy metals solidification in municipal solid waste incineration fly ash. *J. Clean. Prod.* **2023**, *398*, 136642. [CrossRef]
34. Nath, S. Fly ash and zinc slag blended geopolymer: Immobilization of hazardous materials and development of paving blocks. *J. Hazard. Mater.* **2019**, *387*, 121673. [CrossRef] [PubMed]
35. Meskini, S.; Mechnou, I.; Benmansour, M.; Remmal, T.; Samdi, A. Environmental investigation on the use of a phosphogypsum-based road material: Radiological and leaching assessment. *J. Environ. Manag.* **2023**, *345*, 118597. [CrossRef] [PubMed]
36. *GB5085.3-2007*; Identification Standards for Hazardous Wastes Identification for Extraction Toxicity. Beijing Ministry of Ecological Environment of the People's Republic of China: Beijing, China, 2007.
37. Chen, L.; Nakamura, K.; Hama, T. Review on stabilization/solidification methods and mechanism of heavy metals based on OPC-based binders. *J. Environ. Manag.* **2023**, *332*, 117362. [CrossRef] [PubMed]
38. Qiao, G.; Hou, D.; Li, W.; Yin, B.; Zhang, Y.; Wang, P. Molecular insights into migration of heavy metal ion in calcium silicate hydrate (CSH) surface and intra-CSH (Ca/Si = 1.3). *Constr. Build. Mater.* **2023**, *365*, 130097. [CrossRef]
39. Chen, X.; Guo, Y.; Ding, S.; Zhang, H.Y.; Xia, F.Y.; Wang, J.; Zhou, M. Utilization of Red Mud in Geopolymer-based Pervious Concrete with Function of Adsorption of Heavy Metal Ions. *J. Clean. Prod.* **2018**, *207*, 789–800. [CrossRef]
40. Li, Y.; Min, X.; Ke, Y.; Liu, D.; Tang, C. Preparation of red mud-based geopolymer materials from MSWI fly ash and red mud by mechanical activation. *Waste Manag.* **2018**, *83*, 202–208. [CrossRef]

Disclaimer/Publisher's Note: The statements, opinions and data contained in all publications are solely those of the individual author(s) and contributor(s) and not of MDPI and/or the editor(s). MDPI and/or the editor(s) disclaim responsibility for any injury to people or property resulting from any ideas, methods, instructions or products referred to in the content.